NeuroResource

Neuron

Somatic and Dendritic Encoding of Spatial Variables in Retrosplenial Cortex Differs during 2D Navigation

Graphical Abstract

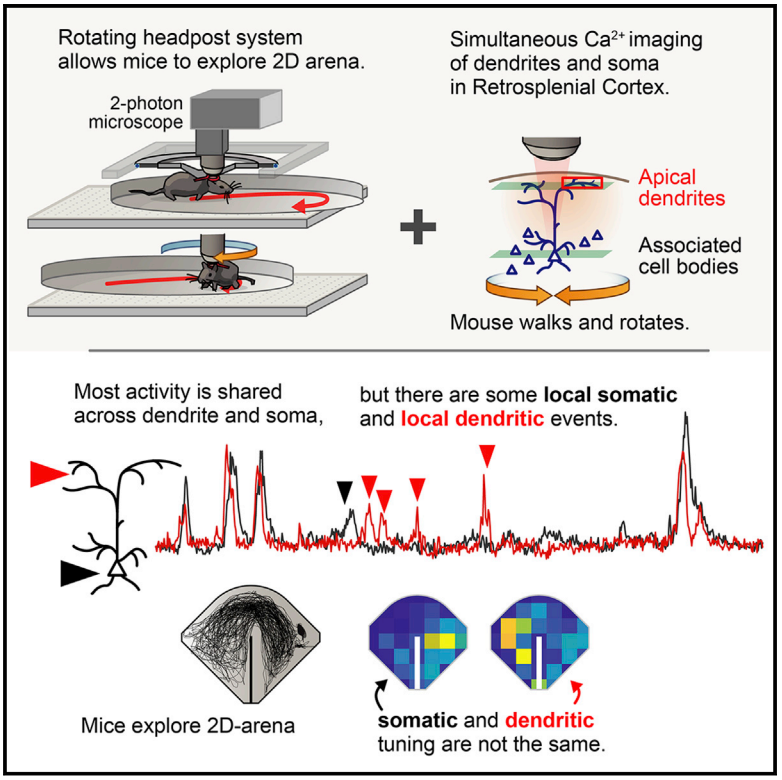

Highlights

- A rotating headpost allows 2-photon imaging in freely locomoting and rotating mice
- Somas and dendrites in retrosplenial cortex showed global and local Ca^{2+} transients
- Local tuft dendritic Ca^{2+} signals were tuned differently from somatic transients

Authors

Jakob Voigts, Mark T. Harnett

Correspondence

harnett@mit.edu

In Brief

Voigts and Harnett present a technology that permits full-featured 2-photon imaging in awake mice during free locomotion with volitional head rotation in a 2D arena and show that local tuft dendritic activity in retrosplenial cortex is not determined solely by somatic activity.

Voigts & Harnett, 2020, Neuron *105*, 237–245
January 22, 2020
https://doi.org/10.1016/j.neuron.2019.10.016

CellPress

Neuron
NeuroResource

Somatic and Dendritic Encoding of Spatial Variables in Retrosplenial Cortex Differs during 2D Navigation

Jakob Voigts[1] and Mark T. Harnett[1,2,*]
[1]Department of Brain & Cognitive Sciences and McGovern Institute for Brain Research, Massachusetts Institute of Technology, Cambridge, MA 02139, USA
[2]Lead Contact
*Correspondence: harnett@mit.edu
https://doi.org/10.1016/j.neuron.2019.10.016

SUMMARY

Active amplification of organized synaptic inputs in dendrites can endow individual neurons with the ability to perform complex computations. However, whether dendrites in behaving animals perform independent local computations is not known. Such activity may be particularly important for complex behavior, where neurons integrate multiple streams of information. Head-restrained imaging has yielded important insights into cellular and circuit function, but this approach limits behavior and the underlying computations. We describe a method for full-featured 2-photon imaging in awake mice during free locomotion with volitional head rotation. We examine head direction and position encoding in simultaneously imaged apical tuft dendrites and their respective cell bodies in retrosplenial cortex, an area that encodes multi-modal navigational information. Activity in dendrites was not determined solely by somatic activity but reflected distinct navigational variables, fulfilling the requirements for dendritic computation. Our approach provides a foundation for studying sub-cellular processes during complex behaviors.

INTRODUCTION

The mammalian cortex combines multiple streams of information to guide behavior; active processing of coincident inputs in the dendrites of neurons has been proposed as a central mechanism for this integration (London and Häusser, 2005; Stuart and Spruston, 2015; Major et al., 2013). However, the relationship between dendritic and somatic receptive fields has been difficult to measure, particularly during complex naturalistic tasks like navigation, which depends on the animal's ability to rotate their head in space (Minderer et al., 2016; Shinder and Taube, 2014; Taube, 2007). In addition to navigation, many complex rodent behaviors (e.g., foraging [Stopka and Macdonald, 2003], olfactory navigation [Gire et al., 2016], and predator avoidance [Yilmaz and Meister, 2013]) are intrinsically spatial and require head and body motion. Current head-fixed behaviors (e.g., sensory stimulus detection [Guo et al., 2014], 2-alternative forced-choice or discrimination [Burgess et al., 2017], and evidence accumulation [Pinto et al., 2018] tasks) lack this complexity. Placing head-fixed rodents on a running wheel, on floating omnidirectional treadmills, or in virtual arenas (Kislin et al., 2014; Nashaat et al., 2016) lacks vestibular input, requires approximation of navigation in 1D (Yoon et al., 2016), and suffers from decreased place cell engagement (Aghajan et al., 2015). These head-fixed approaches are therefore limited in their ability to replicate natural spatial computation or to support higher level cognitive tasks. Virtual reality (VR) (Minderer et al., 2016) methods that allow animals to rotate freely and thus provide vestibular cues have been able to resolve many of these limitations (Aronov and Tank, 2014; Chen et al., 2018) but do not currently allow simultaneous 2-photon imaging.

During navigation, head direction (HD) information is combined with visual and spatial input in the mouse retrosplenial cortex (RSC). Individual RSC neurons in navigating rats exhibit complex conjunctive receptive fields (Alexander and Nitz, 2015, 2017; Clancy et al., 2019; Mao et al., 2017). Anatomical evidence shows that inputs from anterior thalamus (which contains HD cells) make their synapses at distal apical dendrites in RSC (Shibata, 1993). This arrangement suggests that HD inputs may be combined in RSC with other information that is relayed at more peri-somatic synapses via active dendritic processing, similar to what has been described in sensory cortices (Cichon and Gan, 2015; Makino and Komiyama, 2015; Takahashi et al., 2016; Xu et al., 2012; Ranganathan et al., 2018). Calcium imaging has shown that apical dendritic activity can represent behaviorally relevant features (Peters et al., 2017; Ranganathan et al., 2018; Takahashi et al., 2016; Xu et al., 2012), but the extent to which dendritic processing is independent of somatic activity, and therefore could contribute to cortical computation, for example, by allowing single neurons to nonlinearly and hierarchically combine multiple inputs, is unknown. This is particularly true for computations that occur during behaviors in which animals engage in motor actions, as sub-cellular resolution imaging of any brain region has so far only been possible under rigid head fixation.

Here, we developed and applied a new method for 2-photon imaging during free 2D navigation with head rotation. To

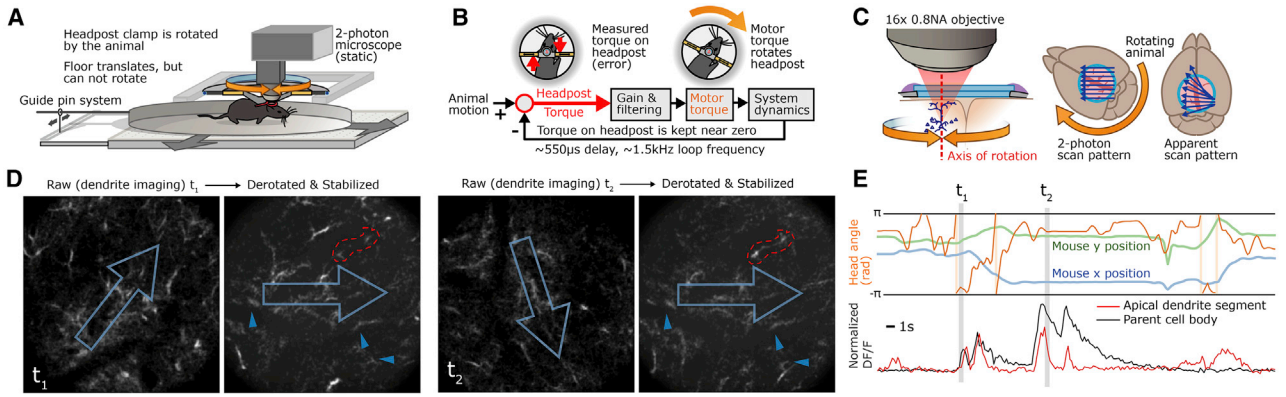

Figure 1. Combining Free Head Rotation with Two-Photon Imaging

(A) Schematic of the method. Mice remain stationary and head fixed but can rotate freely in an active bearing. They walk on a friction-free, translating but non-rotating floor (Figure S1).

(B) An active feedback system measures minute forces applied by the mouse and moves the headpost accordingly, making the bearing appear to have low weight and friction.

(C) A conventional 2-photon microscope stays centered over the brain region of interest and images a rotating field of view.

(D) The resulting images are computationally corrected, making them appear as if recorded from a static animal (Figure S2). The top and bottom rows show the dendritic imaging plane at two time points, at different angles of mouse heading (the concurrently imaged somatic plane is not shown). Dendrite segments remain visible throughout entire rotations, regardless of mouse motion.

(E) Example GCaMP6f traces from a cell body (black) and associated simultaneously recorded apical dendrite segments (red), as well as heading and position traces. GCaMP transients can be observed during fast animal motion and rotation.

See also Figures S1 and S2.

determine whether the conditions for active dendritic processing are met in RSC of behaving mice, we simultaneously imaged dendritic and somatic activity in L5 pyramidal neurons while mice navigated a 2D arena.

RESULTS

Two-Photon Imaging in Locomoting Mice with Free Horizontal Head Rotation

Head-mounted fluorescence microscopes (Aharoni et al., 2019; Ghosh et al., 2011) do not currently permit dendritic or deep multi-plane imaging. Recently, miniaturized two-photon microscopes (Zong et al., 2017) have become available that can perform dendritic imaging during behavior, but these systems are limited in their field of view and ability to image more than one focal plane. We therefore developed an active, animal-actuated rotating headpost that allows mice to engage in 2D navigation and freely turn their head. Mice remain fixed in the azimuthal plane and rotate around the center of the microscope field of view, allowing use of conventional 2-photon imaging. The system consists of a flat air-lifted maze (Kislin et al., 2014; Nashaat et al., 2016) that is prevented from rotating (Figures 1A, S1F, and S1G), and a motorized torque-feedback bearing that allows mice to rotate around a vertical axis while feeling minimal inertia or friction (Figure S1). Mice readily adapt to the system and explore the arena within seconds after first exposure with no overt signs of anxiety (freezing, hunching, walking backward, etc.) typically associated with conventional head fixation (Minderer et al., 2016; Guo et al., 2014; Video S1).

We first evaluated whether the rotating head fixation has an effect on the HD system (Taube, 2007; Taube et al., 1990) by recording HD cells in postsubiculum with chronic tetrode implants (Voigts et al., 2013). We recorded an ensemble of HD coding cells during free exploration of an arena (black circular arena of 25-cm diameter with white cues on one wall; Figure 2A). We then transferred the mice to the head-fixation system (2 meter distance; in the same room), where they were placed in the same circular arena, which now served as the floating floor of the system. We then continued the recording with rotational head fixation. In both settings, mice were enclosed in a box or covered by the ceiling of the head-rotation system and could not see the room outside of the arena. The rotating headpost system had no adverse effect on HD coding in the horizontal plane compared to the freely behaving setting (N = 9 neurons; absolute paired difference in preferred heading computed as circular mean of the firing rate distribution = 3.49 degrees; interquartile range = 19.04 deg; Figure 2A), indicating that our rotating head-fixation method preserves overall function of the HD system.

Despite retained HD coding and fast habituation, our method currently cannot recapitulate the exact kinematics of freely behaving mice and occasional bouts of extremely rapid head rotation. To compare our system to the current state-of-the-art recording methods in freely moving mice, we filmed 4 mice that were implanted with conventional 16-tetrode microdrives with 64-channel headstages and accompanying tether. The tether was not plugged in for these experiments but was suspended from a long thread, eliminating any potential disruption of mouse behavior due to commutator torque or cable twisting. We measured head rotation in the azimuthal plane using camera tracking at 100 Hz. Overall head rotation speeds were largely similar to those in our rotating head-fixed system, though peak rotation speed achieved by the freely moving mice was higher than in our system (Figure 2B; 99th percentiles 9.8 versus 12.5

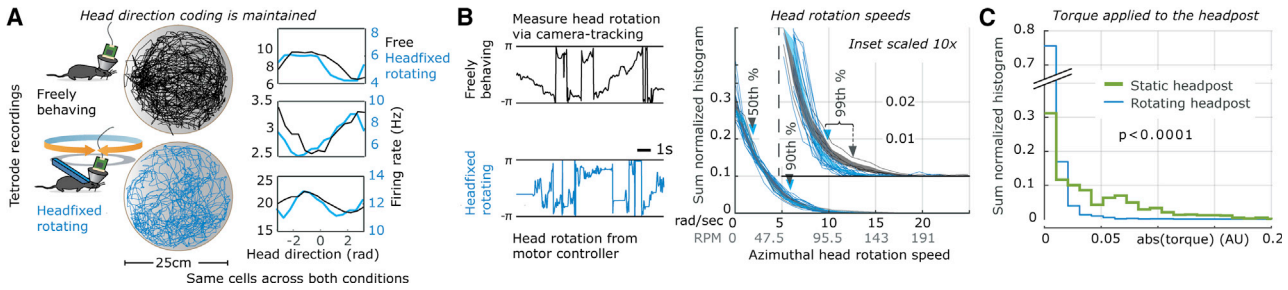

Figure 2. The Mouse-Driven Rotating Head Restraint System Maintains Head Direction Coding

(A) Tetrode recordings in postsubiculum of freely moving and rotating head-fixed mice show that head direction (HD) coding is preserved. Plots show heading-dependent firing rates of three example neurons, recorded in free behavior (black) and rotational head fixation (blue).

(B) Example measurements of head rotation in the azimuthal plane in freely behaving mice with tetrode drives and conventional 64-channel head stages (using camera tracking at 100 Hz) and head rotation in the rotating restraint system (readout from the motor controller). Only time points where the mice walked faster than 5 cm/s were analyzed. Overall head rotation speeds were largely of similar amplitude, but the peak rotation speed achieved by the freely moving mice was higher than the rotation speeds in our system (99th percentiles 9.8 versus 12.5 rad/s; 20 head fixed sessions versus 5 free sessions; $p < 0.05$). Shaded areas indicate 95% confidence interval.

(C) Our method results in less torque felt by the animal than conventional head fixation, which reduces brain motion (histogram of torque values; green, headpost held static, mouse walks back and forth a corridor; blue, our system). This leads to less Z-motion than in conventional systems, evident as a reduction of baseline fluorescence fluctuation in the rotating restraint system compared to static head fixation ($p < 0.005$; Figure S3).

See also Figure S3.

rad/s; 20 headfixed sessions versus 5 free sessions; $p < 0.05$; time points with walking speed >5 cm/s). This difference would likely be more pronounced for mice that carry no implants (or lighter implants) and are capable of moving faster than the drive-implanted animals we used for this comparison, but tethered implants in the 3- to 5-g range represent the currently best available methods for neural recordings in freely behaving mice (Juavinett et al., 2019; Voigts et al., 2013).

Although some existing head-fixed systems allow for forward-backward locomotion on wheels, balls, or treadmills, they all have to counteract the sideways and rotational strain applied by the animals. Even in perfectly stiff headpost mounts, this leads to strain between the rigidly fixed skull and the rest of the animal's body, which can lead to Z-motion (Chen et al., 2013a). In our system, if mice push against the headpost in any direction other than straight upward, the headpost system will give, either by translation of the floor or rotation of the headpost. Upward force is likely small in comparison to the other directions, given that the headpost is positioned ahead of where the mice's paws make contact with the floor, making it hard for mice to push straight up. This results in our method causing less torque applied by the animal than conventional head fixation ($p < 0.0001$; Figure 2C), which reduces the brain motion that is driven by mice applying force to the headpost. This leads to less Z-motion than in conventional systems, evident as a reduction of baseline fluorescence fluctuation (measured as the fluctuation in the 10th percentile of the fluorescence of cell bodies as a function of torque) in the rotating restraint system compared to static head fixation ($p < 0.005$; Figure S3). Brain motion caused by chewing, breathing, and vasomotion should not be affected by our system.

Simultaneous Somatic and Dendritic GCaMP Imaging during Locomotion and Head Rotation

To perform sub-cellular imaging, we virally expressed GCaMP6f (Chen et al., 2013b) in small populations (approximately 50–100 neurons per site) of layer 5 pyramidal neurons of RSC in 5 mice and imaged through chronic windows during free exploration. We performed simultaneous paired imaging of a deep imaging plane containing cell bodies (~350–500 μm below pia) and a superficial imaging plane that transected distal apical tuft dendrite segments (~20–60 μm below the pia) with an electrically tunable lens positioned just before the x/y scan system. We collected data from intermediate distal apical tuft dendrites, branch order 2 and 3 (trunk = 0 order). Mice were imaged during spontaneous exploration of a split arena (Figure 5A). The raw images are rotated and distorted by the interaction between the rotation of the animal and the scan pattern (Figure 1C). We first simultaneously de-rotated and undistorted the raw images by reversing this known scan pattern for each image line in the x-direction individually (Figure S2). We then stabilized the de-rotated images using a standard motion correction pipeline (Pachitariu et al., 2017; Pnevmatikakis and Giovannucci, 2017; Pnevmatikakis et al., 2016). The resulting images are computationally corrected, making them appear as if recorded from a static animal (Figure 1D).

We identified regions of interest (ROIs) for soma and dendrite segments and manually associated paired compartments by tracing along transiently active dendrites in series of Z stacks (Figure S4): for each session, we acquired 50–100 fast Z-scans at ~0.25- to 0.3-Hz repetition rate; these scans are fast enough to capture the entirety of the apical and trunk dendrite in the duration of one GCaMP transient (Figure S4B). By picking Z-scans in which only one or few non-overlapping cells were active, together with the sparse and localized GCaMP expression, this approach allowed us to unambiguously identify which apical tuft dendrites (superficial intermediate and terminal branches) were associated with which somata.

We corrected the $\Delta F/F_0$ traces for angle-dependent brightness changes brought on by small asymmetries in the laser and scan geometry (Figure S5). As an additional safety measure, we restricted analysis to cells for which at least one clear Ca^{2+}

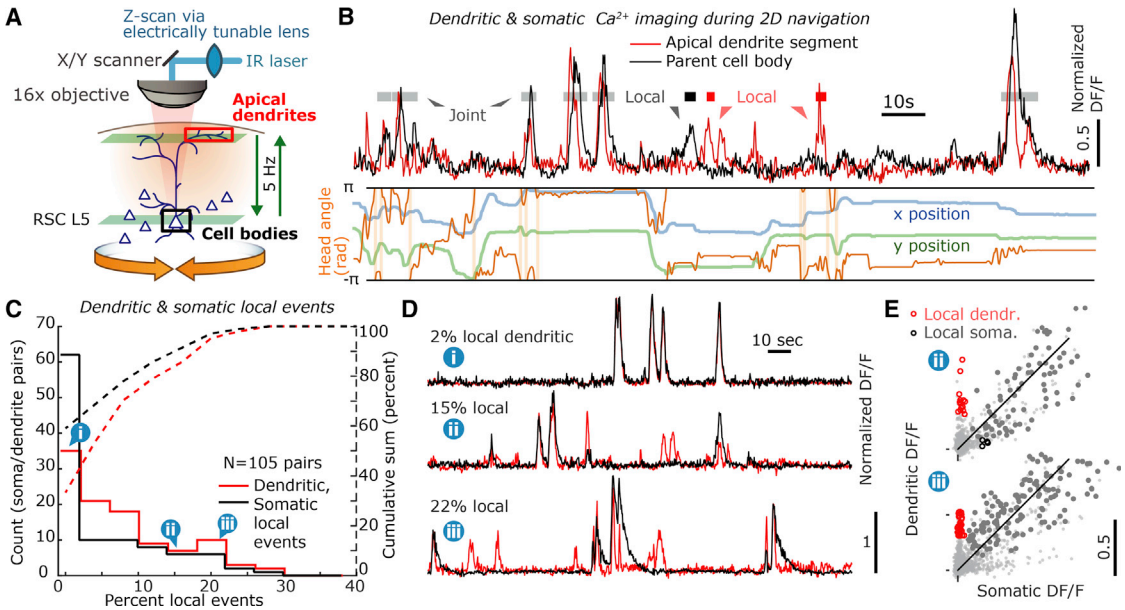

Figure 3. Apical Dendritic GCaMP Events Are Not Fully Mirrored by the Soma

(A) An electrically tunable lens (ETL) alternates between imaging planes for cell bodies and dendrites at 5 Hz, yielding quasi-simultaneous GCaMP imaging of dendrite segments and soma. The dendrite segments are associated with their parent soma in a separate step (Figure S4).

(B) Top: paired GCaMP traces of a L5 dendrite segment (red) and its cell body (black) in RSC, imaged during 2D navigation with free head rotation. Local somatic, local dendritic, and joint transients are indicated with arrows. Bottom: mouse x,y position (green and blue) and heading (orange) are shown.

(C) Histogram of the number of soma/dendrite pairs for different percentages of local GCaMP transients. In 23.8% of dendrites and 16.2% of somas, over 15% of events are independent. Dotted plot, cumulative histogram.

(D) Example GCaMP traces for three representative soma/dendrite pairs from (C).

(E) Example scatterplots of the somatic versus dendritic normalized GCaMP signals (traces were low-pass filtered with a Gaussian filter; σ = 0.6 s). Circles in red/black show maximum amplitudes per events. Grey dots represent the entire raw traces (every 15th sample is plotted).

See also Figure S4.

transient (or decay of a transient) was visible in all four 90° orientation segments (to be able to judge that they had comparable brightness). This selection is not strictly necessary and could be safely omitted when using a microscope with a stable, well-calibrated scan geometry. We also excluded cells where the appearance of the dendritic ROI changed between isolated and joint events (to exclude possible contamination from another overlapping dendrite segment), leaving N = 105 soma/dendrite pairs. We normalized dendritic and somatic traces by amplitude and detected GCaMP events by computing and comparing against the noise distribution (estimated via quantiles in the normalized ΔF/F data). Events were detected via the product of the noise probabilities for the somatic and dendritic time series (onset threshold P(noise) < 20%), which labels events originating from either or from both of the traces. We then classified events as dendritic only (dendritic > somatic event amplitude and no detectable somatic transient), somatic only (same but reversed), or joint events (all other—see STAR Methods).

Somatic and Dendritic GCaMP Transients

We found that the majority of dendritic GCaMP transients coincided with somatic transients, indicating they could result from coordinated somato-dendritic activity (Helmchen et al., 1999; Hill et al., 2013; Stuart and Spruston, 2015; Figure 3B). However, a significant fraction of soma-dendrite pairs exhibit local dendritic events (Figure 3), showing that regenerative Ca^{2+}-dependent processing (Cichon and Gan, 2015; London and Häusser, 2005; Palmer et al., 2014) in distal apical tuft dendrites does not necessarily lead to somatic Ca^{2+} activity in awake-behaving mice. We also observed somatic events with no associated GCaMP transient in the apical tuft segment (Figures 3B and 3C), indicating that somatic spiking does not necessarily invade the entire dendritic arbor, either due to dendritic voltage attenuation (Harnett et al., 2013; Helmchen et al., 1999; Stuart and Häusser, 2001; Stuart and Sakmann, 1994) or inhibition (Larkum et al., 1999; Murayama et al., 2009; Palmer et al., 2012).

Local events were on average smaller (Figure 5A) and faster (Figure 5B) than joint events. The total scan speed of our 2-photon system was 10 Hz. Each imaging plane was therefore scanned at 5 Hz (Figure 3A). We analyzed simulated data to determine whether this sample rate is expected to lead to a significant percentage of missed $Ca2^{+}$ transients. Transients were simulated at 1 kHz, as σ = 0.1 s Gaussians, convolved with exponential decay filters of varying timescales of τ = 0.1–1 s (Figure 4C). The event amplitudes were set at 0.5 (a.u.), and events were detected using a threshold of 0.3. This value represents a conservative choice, where amplitude losses of 40% will lead to a failure to detect the event. We then calculated the proportion of missed events for decay time constants of τ between 0.1 s and 1 s. Within the range of observed time constants for GCaMP

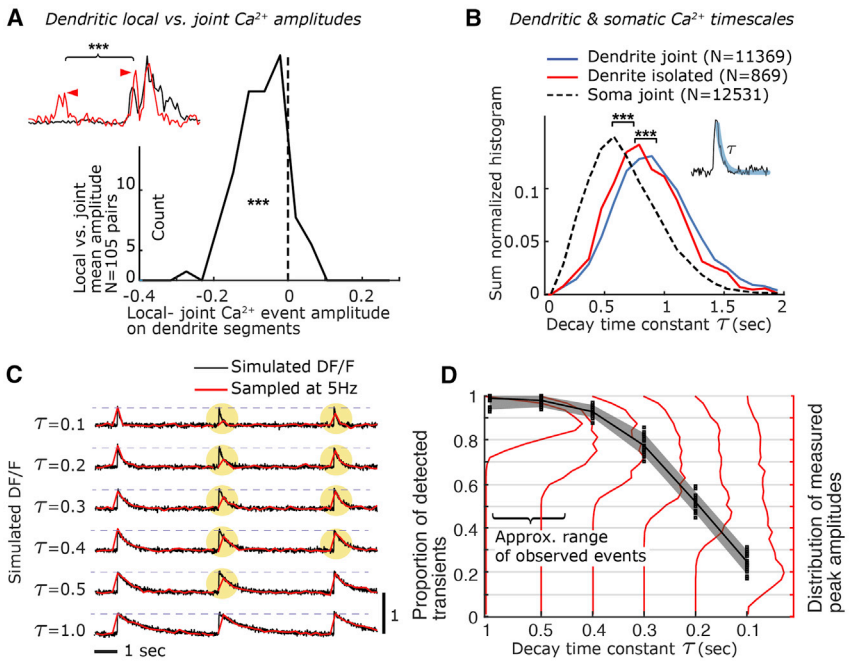

Figure 4. Apical Dendritic GCaMP Events Are Faster and Smaller Than Somatic GCaMP Transients

(A) Histogram of relative dendritic GCaMP event amplitudes for local versus joint events. Independent events are smaller than joint events. Inset shows example independent and joint transients.

(B) Histogram of GCaMP event decay time constants. Dendritic transients are faster than somatic transients, and independent dendritic transients (without coincident somatic transient) are faster than joint ones.

(C) Simulated GCaMP data (black), sampled at 5 Hz (red) of various event decay timescales of τ = 0.1–1 s. At faster decay times, the apparent sampled event amplitudes can appear smaller than the true amplitudes, leading to some events being missed by the threshold (yellow circles).

(D) Proportion of detected events (max. event amplitude = 0.5; detection threshold = 0.3) for the decay time constants in (C) (black, shaded area represents 90% quantiles of 20 simulated datasets). Within the range of observed time constants for events in the soma or dendrites (τ > 0.4 s; B), over 90% of true events are expected to be observable. Red, distribution of peak amplitudes detected in the 5-Hz sampled data relative to true peak amplitude (sum normalized histograms).

events in the soma or dendrites ($\tau > 0.4$ s; Figure 4B), over 90% of true events are expected to be observable (Figure 4D).

Somatic and Dendritic Encoding of Spatial Variables Differ during 2D Navigation

To assess how local dendritic transients could contribute to subcellular computation, we compared somatic and dendritic tuning during free exploration of a split area (Figure 5A; Video S2). To compute spatial and HD tuning, GCaMP event rates were computed by dividing event count by occupancy in an 8 × 8 grid for the position (Figure 5D) and 40 bins, circularly smoothed with σ = 0.075 radians for HD, excluding times when the mouse was stationary. To compute the information content of the tuning, the entropy of the spatial and HD rate distributions was computed as the Kullback-Leibler (KL) divergence between the distribution of rates and the distribution of occupancy, giving us a measure of whether and how much additional information is contained in the firing rate pattern in addition to the information contained in the statistics of the mouse's behavior (see STAR Methods). The amount of position and HD information content in local dendritic and somatic signals are similar (entropy differences $p > 0.2$; see STAR Methods), showing that local dendritic activity is not generally more or less sharply tuned than the somatic output.

However, the local dendritic and somatic tuning differ from each other in what spatial and HD distributions they coded for. We assessed this by converting both time series to point processes by detecting GCaMP transients (see STAR Methods), removing information carried by amplitude and dynamics. We then matched the rates of both (via resampling). The resulting time series is free of potential confounds of different GCaMP timescales and rates between the compartments (Figure 5E).

We then compared the spatial and HD tuning of local dendritic events to themselves across different halves of the experiment (as control for variance, to test how reliable the coding itself was) or to the somatic events across the same halves of the experiment (split in 15-min chunks; Figure 5E). The somatic tuning differed more from the dendritic tuning than the dendritic tuning from itself (Figure 5F; $p < 0.005$ for both HD and position), showing that dendritic tuning is reliable and capable of independence and that it differs from the tuning of their parent somata. We also found that pairs of dendrites originating from the same soma (Figure 5D, example on the right) differed in their position tuning ($p = 0.010$), but not significantly in HD tuning ($p = 0.153$; N = 12 cells, 14 branch-to-branch comparisons; same method as before but comparing branches to themselves or other branches on the same cell). This indicates that local activity in apical dendrites of L5 pyramidal cells in RSC reflects not just a failure of these events to elicit somatic spiking but instead that they encode navigational variables differently from their parent soma.

DISCUSSION

Here, we report the development of an animal-actuated rotating headpost that makes it possible to combine methods that require head fixation, such as conventional 2-photon imaging, with animal locomotion and head rotation. By providing true vestibular cues to the animals, this system removes much of the discomfort and resulting unnatural behavior associated with existing head-fixed approaches. Using this approach, we found that local activity in apical dendrites of L5 pyramidal cells in RSC is not tightly linked to somatic activity. Further, this local dendritic activity reflects navigational variables in a way that

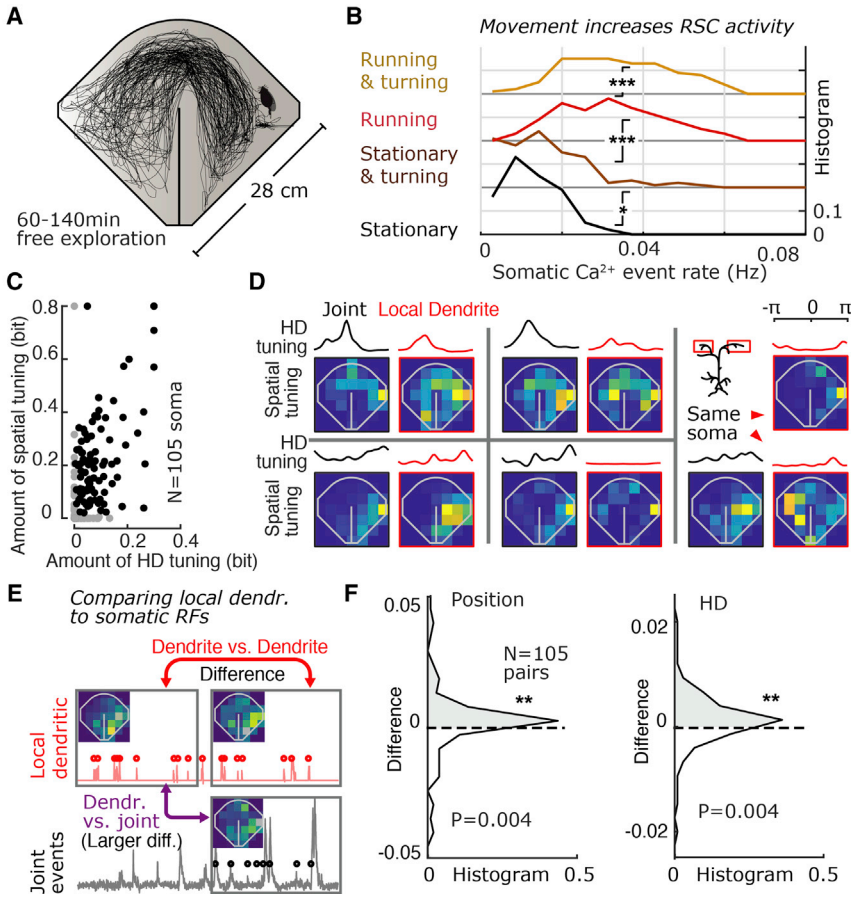

Figure 5. Isolated Dendritic Activity Is Tuned Differently Than Its Parent Soma

(A) Experiment schematic: mice freely explore a split arena.

(B) Somatic firing rates (measured as GCaMP event rate) in RSC L5 increase with head rotation and with locomotion (rank sum, 5 mice, 105 L5 RSC cell bodies).

(C) Distribution of location and HD tuning of L5 pyramidal cells in RSC, quantified in bits (see STAR Methods). Cells show a variety of HD and location tunings (black, cells tuned in both dimensions; gray, tuned in only one, assessed via the entropy of the cells tuning versus the entropy of the mouse's occupancy).

(D) Examples of spatial and HD tuning of the dendrites (right, red) and their parent soma (left, black). The last example shows two dendrite segments of the same soma that have different spatial and HD coding.

(E) Joint and local dendritic events are converted to point processes, removing any GCaMP dynamics that could differ systematically between soma and dendrite, and then rate matched by resampling. We then compared the spatial and HD tuning of the resulting point processes for local dendritic events (red) to themselves in non-overlapping windows (to establish a baseline for tuning reliability) and to the tuning of the parent soma (purple) in the same time window. The dendrite/soma difference was significantly higher than dendrite/dendrite difference, showing that the tuning of local dendritic events differs from their soma.

(F) Difference statistics (signed-rank test; soma/dendrite difference - dendrite/dendrite difference) for position and HD tuning.

does not fully mirror the tuning of the parent soma (Figure 5). This finding indicates that active dendritic mechanisms (London and Häusser, 2005; Magee, 2000; Major et al., 2013; Stuart and Spruston, 2015) could work together with network mechanisms to implement cortical computations in RSC.

Active Dendritic Computation

Calcium imaging of dendrites has shown that active dendritic processes represent behaviorally relevant features in task-performing animals (Peters et al., 2017; Takahashi et al., 2016; Xu et al., 2012; Ranganathan et al., 2018), but it is not clear whether such dendritic activity is coincident with somatic activity, is inherited from somatic bursting via backpropagation into the dendrite, or is independent. To date, most simultaneous measurements of dendritic and somatic Ca^{2+} activity in behaving animals have found a high degree of correlation of their activity (Beaulieu-Laroche et al., 2019; Peters et al., 2017), suggesting a tight functional coupling of dendritic activity to somatic spiking output. The majority of these measurements were made in primary sensory (Beaulieu-Laroche et al., 2019; Ranganathan et al., 2018) or motor (Peters et al., 2017) cortex trunk dendrites that have a higher degree of electrical coupling to the soma than distal apical tuft branches.

Local dendritic NMDA spikes have been observed in tuft dendrites in response to sensory input in L2/3 cells *in vivo* and have been shown to play a role in relaying dendritic input to the soma (Cichon and Gan, 2015; Palmer et al., 2014). More recent studies employing simultaneous multi-plane imaging have observed some independent activity in distal apical tuft dendrites and soma during behavior (Francioni and Rochefort, 2019; Kerlin et al., 2018). Observations in L5 of anterior lateral motor cortex during decision making revealed comparable proportions of local dendritic transients to what we observed (Kerlin et al., 2018) but without significant soma-only activity. In contrast, measurements of L5 activity in V1 during awake presentation of visual stimuli showed GCaMP activity that was localized to the soma but failed to propagate to the apical tuft (Francioni and Rochefort, 2019). In our experiments in L5 cells in RSC of navigating mice, we found both types of local activity (Figure 3). We also found limited evidence for the independence of spikes across different branches of the same cells. Branch-specific activity in distal tuft dendrites has been observed in motor learning (Cichon and Gan, 2015), but not in primary somatosensory cortex during active whisking (Xu et al., 2012). These divergent observations of prevalence, coincidence, and spread of local dendritic activity could be the result of a few differences between the studies: different brain regions (pre-motor, associative, and primary sensory) could perform their respective computations differently, and different computational and behavioral states have been shown to modulate the electrical coupling between

somata and dendrites (Helmchen et al., 1999) via changes in inhibitory activity (Larkum et al., 1999; Silberberg and Markram, 2007; Takahashi et al., 2016) or neuromodulatory state (Brombas et al., 2014; Labarrera et al., 2018; Williams and Fletcher, 2019). All of these could be driven by different neural activity patterns, different levels of top-down versus bottom-up activity, and/or local neuromodulation across different cortical regions and tasks. Our finding underlines the importance of studying dendritic computation in the context of behaviors that sufficiently engage the respective cortical circuitry.

Despite the high sensitivity and fast timescale of GCaMP6f, low-frequency somatic action potentials might not lead to detectable fluorescence transients in L5 pyramidal neurons (Beaulieu-Laroche et al., 2019). Similarly, earlier work found detectable changes in dendritic Ca^{2+} only with high-frequency somatic spiking, using dye-based indicators (Helmchen et al., 1999). This potential limitation of Ca^{2+} imaging, and specifically of GCaMP, implies that the local somatic events we detected (Figures 3 and 4) could represent short bursts that fail to elicit a dendritic GCaMP transient rather than individual somatic spikes. This would imply that there is a baseline of currently unobservable low-frequency spiking that is less likely to affect apical dendritic voltage than bursts and suggests a potentially higher degree of functional independence between apical dendrites and soma than indicated by Ca^{2+} imaging. Next-generation voltage imaging (Abdelfattah et al., 2019; Adam et al., 2019; Xu et al., 2017) could directly address this in the future.

RSC encodes conjunctions of navigational variables, for example, HD encoding that changes with position (Alexander and Nitz, 2015; Jacob et al., 2017). Our observation of differences in dendritic and somatic tuning shows that this mixing of variables could be a function of dendritic processing (London and Häusser, 2005; Stuart and Spruston, 2015). The different types of receptive fields in RSC (Alexander and Nitz, 2015, 2017; Jacob et al., 2017; Mao et al., 2017) may correlate with differences in the contribution of dendritic processing to the somatic output. Spiking of an RSC neuron with tuning for purely visual information could, for example, be determined predominantly by peri-somatic input, while the activity in another neuron that encodes heading only in a specific spatial context could be the result of nonlinear dendritic amplification of select coincident inputs. The localized dendritic Ca^{2+} transients that we observe here do not merely reflect failures of synaptic input to elicit somatic activation but instead are tuned differently from the somatic output of the neurons (Figure 5). This shows that the conditions for complex dendritic computation (London and Häusser, 2005; Magee, 2000; Stuart and Spruston, 2015) are fulfilled in RSC. Our observations suggest that active dendritic processes nonlinearly combine HD and other inputs in RSC to give rise to its large diversity of egocentric and allocentric spatial encoding schemes (Alexander and Nitz, 2015, 2017).

Other Applications of the Technology

Our method for combining head-fixed methods with free head rotation and locomotion places no restrictions on the use of optical methods, such as patterned stimulation (Adam et al., 2019; Forli et al., 2018; Zhang et al., 2018), and is compatible with additional instruments of considerable weight attached to the rotating headpost frame, such as Neuropixels probes (Jun et al., 2017; Steinmetz et al., 2018), manipulators for whole-cell recording (Margrie et al., 2002; Harvey et al., 2009; Zhou et al., 2014), or any high-channel count probes that require large amounts of local amplification or digitization electronics (Hong and Lieber, 2019; Joo et al., 2019; Yang et al., 2019). Practically, instrumentation exceeding a few kilograms will require more costly drive motors and bearings, although the remainder of the system can be replicated as described here. Reward delivery, videography, light delivery for optogenetics, electrical stimulation, etc., can all similarly be integrated with minimal modifications. By removing many of the limitations that head fixation places on animal behavior, our approach should have broad utility for the study of navigation as well as for investigations of complex cognitive behaviors (Carandini and Churchland, 2013; Hoy et al., 2016; Karlsson et al., 2012) in rodents.

STAR★METHODS

Detailed methods are provided in the online version of this paper and include the following:

- KEY RESOURCES TABLE
- LEAD CONTACT AND MATERIALS AVAILABILITY
- EXPERIMENTAL MODEL AND SUBJECT DETAILS
- METHOD DETAILS
  - Mechanical system
  - Force feedback control system
  - Surgery
  - Chronic Electrophysiology
  - 2-Photon imaging
  - De-rotation
  - Correction of uneven illumination
  - Identification and classification of Ca^{2+} transients
- QUANTIFICATION AND STATISTICAL ANALYSIS
- DATA AND CODE AVAILABILITY

SUPPLEMENTAL INFORMATION

Supplemental Information can be found online at https://doi.org/10.1016/j.neuron.2019.10.016.

ACKNOWLEDGMENTS

We thank Jonathan P. Newman for many helpful discussions and technical advice. We thank Matt Wilson for helpful discussions and Lou Beaulieu-Laroche, Lukas Fischer, Marie-Sophie van der Goes, Enrique Toloza, Laura Lewis, Ben Scott, Courtney Yaeger, and Michael R. Tadross for comments on the manuscript. Funding was provided from the MIT NEC Corporation Fund for Research in Computers and Communications and the NIH (R01NS106031 and R21NS103098; to M.T.H.). M.T.H. is a Klingenstein-Simons Fellow in Neuroscience, a Vallee Foundation Scholar, and a McKnight Scholar; J.V. is a Simons Center for the Social Brain at MIT postdoctoral fellow.

AUTHOR CONTRIBUTIONS

Conceptualization, J.V. and M.T.H.; Methodology, J.V.; Software, J.V.; Investigation, J.V.; Writing – Original Draft, J.V.; Writing – Review & Editing, J.V. and M.T.H.; Visualization, J.V.; Funding Acquisition, J.V. and M.T.H.; Resources, J.V. and M.T.H.; Supervision, M.T.H.

DECLARATION OF INTERESTS

The authors declare no competing interests.

Received: May 9, 2019
Revised: August 14, 2019
Accepted: October 9, 2019
Published: November 20, 2019

REFERENCES

Abdelfattah, A.S., Kawashima, T., Singh, A., Novak, O., Liu, H., Shuai, Y., Huang, Y.-C., Campagnola, L., Seeman, S.C., Yu, J., et al. (2019). Bright and photostable chemigenetic indicators for extended in vivo voltage imaging. Science *365*, 699–704.

Adam, Y., Kim, J.J., Lou, S., Zhao, Y., Xie, M.E., Brinks, D., Wu, H., Mostajo-Radji, M.A., Kheifets, S., Parot, V., et al. (2019). Voltage imaging and optogenetics reveal behaviour-dependent changes in hippocampal dynamics. Nature *569*, 413–417.

Aghajan, Z.M., Acharya, L., Moore, J.J., Cushman, J.D., Vuong, C., and Mehta, M.R. (2015). Impaired spatial selectivity and intact phase precession in two-dimensional virtual reality. Nat. Neurosci. *18*, 121–128.

Aharoni, D., Khakh, B.S., Silva, A.J., and Golshani, P. (2019). All the light that we can see: a new era in miniaturized microscopy. Nat. Methods *16*, 11–13.

Alexander, A.S., and Nitz, D.A. (2015). Retrosplenial cortex maps the conjunction of internal and external spaces. Nat. Neurosci. *18*, 1143–1151.

Alexander, A.S., and Nitz, D.A. (2017). Spatially periodic activation patterns of retrosplenial cortex encode route sub-spaces and distance traveled. Curr. Biol. *27*, 1551–1560.e4.

Andermann, M.L., Kerlin, A.M., Roumis, D.K., Glickfeld, L.L., and Reid, R.C. (2011). Functional specialization of mouse higher visual cortical areas. Neuron *72*, 1025–1039.

Andermann, M.L., Gilfoy, N.B., Goldey, G.J., Sachdev, R.N.S., Wölfel, M., McCormick, D.A., Reid, R.C., and Levene, M.J. (2013). Chronic cellular imaging of entire cortical columns in awake mice using microprisms. Neuron *80*, 900–913.

Aronov, D., and Tank, D.W. (2014). Engagement of neural circuits underlying 2D spatial navigation in a rodent virtual reality system. Neuron *84*, 442–456.

Beaulieu-Laroche, L., Toloza, E.H.S., Brown, N.J., and Harnett, M.T. (2019). Widespread and highly correlated somato-dendritic activity in cortical layer 5 neurons. Neuron *103*, 235–241.e4.

Brombas, A., Fletcher, L.N., and Williams, S.R. (2014). Activity-dependent modulation of layer 1 inhibitory neocortical circuits by acetylcholine. J. Neurosci. *34*, 1932–1941.

Burgess, C.P., Lak, A., Steinmetz, N.A., Zatka-Haas, P., Bai Reddy, C., Jacobs, E.A.K., Linden, J.F., Paton, J.J., Ranson, A., Schröder, S., et al. (2017). High-yield methods for accurate two-alternative visual psychophysics in head-fixed mice. Cell Rep. *20*, 2513–2524.

Carandini, M., and Churchland, A.K. (2013). Probing perceptual decisions in rodents. Nat. Neurosci. *16*, 824–831.

Chen, J.L., Pfäffli, O.A., Voigt, F.F., Margolis, D.J., and Helmchen, F. (2013a). Online correction of licking-induced brain motion during two-photon imaging with a tunable lens. J. Physiol. *591*, 4689–4698.

Chen, T.-W., Wardill, T.J., Sun, Y., Pulver, S.R., Renninger, S.L., Baohan, A., Schreiter, E.R., Kerr, R.A., Orger, M.B., Jayaraman, V., et al. (2013b). Ultrasensitive fluorescent proteins for imaging neuronal activity. Nature *499*, 295–300.

Chen, G., King, J.A., Lu, Y., Cacucci, F., and Burgess, N. (2018). Spatial cell firing during virtual navigation of open arenas by head-restrained mice. eLife *7*, e34789.

Cichon, J., and Gan, W.-B. (2015). Branch-specific dendritic Ca(2+) spikes cause persistent synaptic plasticity. Nature *520*, 180–185.

Clancy, K.B., Orsolic, I., and Mrsic-Flogel, T.D. (2019). Locomotion-dependent remapping of distributed cortical networks. Nat. Neurosci. *22*, 778–786.

Forli, A., Vecchia, D., Binini, N., Succol, F., Bovetti, S., Moretti, C., Nespoli, F., Mahn, M., Baker, C.A., Bolton, M.M., et al. (2018). Two-photon bidirectional control and imaging of neuronal excitability with high spatial resolution in vivo. Cell Rep. *22*, 3087–3098.

Francioni, V., and Rochefort, N.L. (2019). High and asymmetric somato-dendritic coupling of V1 layer 5 neurons independent of behavioural state and visual stimulation. bioRxiv. https://doi.org/10.1101/664177.

Ghosh, K.K., Burns, L.D., Cocker, E.D., Nimmerjahn, A., Ziv, Y., Gamal, A.E., and Schnitzer, M.J. (2011). Miniaturized integration of a fluorescence microscope. Nat. Methods *8*, 871–878.

Gire, D.H., Kapoor, V., Arrighi-Allisan, A., Seminara, A., and Murthy, V.N. (2016). Mice develop efficient strategies for foraging and navigation using complex natural stimuli. Curr. Biol. *26*, 1261–1273.

Goldey, G.J., Roumis, D.K., Glickfeld, L.L., Kerlin, A.M., Reid, R.C., Bonin, V., Schafer, D.P., and Andermann, M.L. (2014). Removable cranial windows for long-term imaging in awake mice. Nat. Protoc. *9*, 2515–2538.

Guo, Z.V., Hires, S.A., Li, N., O'Connor, D.H., Komiyama, T., Ophir, E., Huber, D., Bonardi, C., Morandell, K., Gutnisky, D., et al. (2014). Procedures for behavioral experiments in head-fixed mice. PLoS ONE *9*, e88678.

Harnett, M.T., Xu, N.-L., Magee, J.C., and Williams, S.R. (2013). Potassium channels control the interaction between active dendritic integration compartments in layer 5 cortical pyramidal neurons. Neuron *79*, 516–529.

Harvey, C.D., Collman, F., Dombeck, D.A., and Tank, D.W. (2009). Intracellular dynamics of hippocampal place cells during virtual navigation. Nature *461*, 941–946.

Helmchen, F., Svoboda, K., Denk, W., and Tank, D.W. (1999). In vivo dendritic calcium dynamics in deep-layer cortical pyramidal neurons. Nat. Neurosci. *2*, 989–996.

Hill, D.N., Varga, Z., Jia, H., Sakmann, B., and Konnerth, A. (2013). Multibranch activity in basal and tuft dendrites during firing of layer 5 cortical neurons in vivo. Proc. Natl. Acad. Sci. USA *110*, 13618–13623.

Hong, G., and Lieber, C.M. (2019). Novel electrode technologies for neural recordings. Nat. Rev. Neurosci. *20*, 330–345.

Hoy, J.L., Yavorska, I., Wehr, M., and Niell, C.M. (2016). Vision drives accurate approach behavior during prey capture in laboratory mice. Curr. Biol. *26*, 3046–3052.

Jacob, P.-Y., Casali, G., Spieser, L., Page, H., Overington, D., and Jeffery, K. (2017). An independent, landmark-dominated head-direction signal in dysgranular retrosplenial cortex. Nat. Neurosci. *20*, 173–175.

Ji, N., Magee, J.C., and Betzig, E. (2008). High-speed, low-photodamage nonlinear imaging using passive pulse splitters. Nat. Methods *5*, 197–202.

Joo, H.R., Fan, J.L., Chen, S., Pebbles, J.A., Liang, H., Chung, J.E., Yorita, A.M., Tooker, A., Tolosa, V., Geaghan-Breiner, C., et al. (2019). A microfabricated, 3D-sharpened silicon shuttle for insertion of flexible electrode arrays through dura mater into brain. J. Neural Eng. Published online June 19, 2019. https://doi.org/10.1088/1741-2552/ab2b2e.

Juavinett, A.L., Bekheet, G., and Churchland, A.K. (2019). Chronically implanted Neuropixels probes enable high-yield recordings in freely moving mice. eLife *8*, e47188.

Jun, J.J., Steinmetz, N.A., Siegle, J.H., Denman, D.J., Bauza, M., Barbarits, B., Lee, A.K., Anastassiou, C.A., Andrei, A., Aydın, Ç., et al. (2017). Fully integrated silicon probes for high-density recording of neural activity. Nature *551*, 232–236.

Karlsson, M.P., Tervo, D.G.R., and Karpova, A.Y. (2012). Network resets in medial prefrontal cortex mark the onset of behavioral uncertainty. Science *338*, 135–139.

Kerlin, A., Mohar, B., Flickinger, D., MacLennan, B.J., Davis, C., Spruston, N., and Svoboda, K. (2018). Functional clustering of dendritic activity during decision-making. bioRxiv. https://doi.org/10.1101/440396.

Kislin, M., Mugantseva, E., Molotkov, D., Kulesskaya, N., Khirug, S., Kirilkin, I., Pryazhnikov, E., Kolikova, J., Toptunov, D., Yuryev, M., et al. (2014). Flat-floored air-lifted platform: a new method for combining behavior with microscopy or electrophysiology on awake freely moving rodents. J. Vis. Exp. e51869.

Labarrera, C., Deitcher, Y., Dudai, A., Weiner, B., Kaduri Amichai, A., Zylbermann, N., and London, M. (2018). Adrenergic modulation regulates the dendritic excitability of layer 5 pyramidal neurons in vivo. Cell Rep. *23*, 1034–1044.

Larkum, M.E., Zhu, J.J., and Sakmann, B. (1999). A new cellular mechanism for coupling inputs arriving at different cortical layers. Nature *398*, 338–341.

London, M., and Häusser, M. (2005). Dendritic computation. Annu. Rev. Neurosci. *28*, 503–532.

Magee, J.C. (2000). Dendritic integration of excitatory synaptic input. Nat. Rev. Neurosci. *1*, 181–190.

Major, G., Larkum, M.E., and Schiller, J. (2013). Active properties of neocortical pyramidal neuron dendrites. Annu. Rev. Neurosci. *36*, 1–24.

Makino, H., and Komiyama, T. (2015). Learning enhances the relative impact of top-down processing in the visual cortex. Nat. Neurosci. *18*, 1116–1122.

Mao, D., Kandler, S., McNaughton, B.L., and Bonin, V. (2017). Sparse orthogonal population representation of spatial context in the retrosplenial cortex. Nat. Commun. *8*, 243.

Margrie, T.W., Brecht, M., and Sakmann, B. (2002). In vivo, low-resistance, whole-cell recordings from neurons in the anaesthetized and awake mammalian brain. Pflugers Arch. *444*, 491–498.

Minderer, M., Harvey, C.D., Donato, F., and Moser, E.I. (2016). Neuroscience: virtual reality explored. Nature *533*, 324–325.

Murayama, M., Pérez-Garci, E., Nevian, T., Bock, T., Senn, W., and Larkum, M.E. (2009). Dendritic encoding of sensory stimuli controlled by deep cortical interneurons. Nature *457*, 1137–1141.

Nashaat, M.A., Oraby, H., Sachdev, R.N.S., Winter, Y., and Larkum, M.E. (2016). Air-Track: a real-world floating environment for active sensing in head-fixed mice. J. Neurophysiol. *116*, 1542–1553.

Nashaat, M.A., Oraby, H., Peña, L.B., Dominiak, S., Larkum, M.E., and Sachdev, R.N.S. (2017). Pixying behavior: a versatile real-time and post hoc automated optical tracking method for freely moving and head fixed animals. eNeuro *4*, ENEURO.0245-16.2017.

Newman, J.P., Fong, M.F., Millard, D.C., Whitmire, C.J., Stanley, G.B., and Potter, S.M. (2015). Optogenetic feedback control of neural activity. eLife *4*, e07192.

Pachitariu, M., Stringer, C., Dipoppa, M., Schröder, S., Rossi, L.F., Dalgleish, H., Carandini, M., and Harris, K.D. (2017). Suite2p: beyond 10,000 neurons with standard two-photon microscopy. bioRxiv. https://doi.org/10.1101/061507.

Palmer, L., Murayama, M., and Larkum, M. (2012). Inhibitory regulation of dendritic activity in vivo. Front. Neural Circuits *6*, 26.

Palmer, L.M., Shai, A.S., Reeve, J.E., Anderson, H.L., Paulsen, O., and Larkum, M.E. (2014). NMDA spikes enhance action potential generation during sensory input. Nat. Neurosci. *17*, 383–390.

Peters, A.J., Lee, J., Hedrick, N.G., O'Neil, K., and Komiyama, T. (2017). Reorganization of corticospinal output during motor learning. Nat. Neurosci. *20*, 1133–1141.

Peyrache, A., Lacroix, M.M., Petersen, P.C., and Buzsáki, G. (2015). Internally organized mechanisms of the head direction sense. Nat. Neurosci. *18*, 569–575.

Pinto, L., Koay, S.A., Engelhard, B., Yoon, A.M., Deverett, B., Thiberge, S.Y., Witten, I.B., Tank, D.W., and Brody, C.D. (2018). An accumulation-of-evidence task using visual pulses for mice navigating in virtual reality. Front. Behav. Neurosci. *12*, 36.

Pnevmatikakis, E.A., and Giovannucci, A. (2017). NoRMCorre: an online algorithm for piecewise rigid motion correction of calcium imaging data. J. Neurosci. Methods *291*, 83–94.

Pnevmatikakis, E.A., Soudry, D., Gao, Y., Machado, T.A., Merel, J., Pfau, D., Reardon, T., Mu, Y., Lacefield, C., Yang, W., et al. (2016). Simultaneous denoising, deconvolution, and demixing of calcium imaging data. Neuron *89*, 285–299.

Ranganathan, G.N., Apostolides, P.F., Harnett, M.T., Xu, N.-L., Druckmann, S., and Magee, J.C. (2018). Active dendritic integration and mixed neocortical network representations during an adaptive sensing behavior. Nat. Neurosci. *21*, 1583–1590.

Shibata, H. (1993). Efferent projections from the anterior thalamic nuclei to the cingulate cortex in the rat. J. Comp. Neurol. *330*, 533–542.

Shinder, M.E., and Taube, J.S. (2014). Resolving the active versus passive conundrum for head direction cells. Neuroscience *270*, 123–138.

Siegle, J.H., López, A.C., Patel, Y.A., Abramov, K., Ohayon, S., and Voigts, J. (2017). Open Ephys: an open-source, plugin-based platform for multichannel electrophysiology. J. Neural Eng. *14*, 045003.

Silberberg, G., and Markram, H. (2007). Disynaptic inhibition between neocortical pyramidal cells mediated by Martinotti cells. Neuron *53*, 735–746.

Steinmetz, N.A., Koch, C., Harris, K.D., and Carandini, M. (2018). Challenges and opportunities for large-scale electrophysiology with Neuropixels probes. Curr. Opin. Neurobiol. *50*, 92–100.

Stopka, P., and Macdonald, D.W. (2003). Way-marking behaviour: an aid to spatial navigation in the wood mouse (Apodemus sylvaticus). BMC Ecol. *3*, 3.

Stuart, G.J., and Häusser, M. (2001). Dendritic coincidence detection of EPSPs and action potentials. Nat. Neurosci. *4*, 63–71.

Stuart, G.J., and Sakmann, B. (1994). Active propagation of somatic action potentials into neocortical pyramidal cell dendrites. Nature *367*, 69–72.

Stuart, G.J., and Spruston, N. (2015). Dendritic integration: 60 years of progress. Nat. Neurosci. *18*, 1713–1721.

Takahashi, N., Oertner, T.G., Hegemann, P., and Larkum, M.E. (2016). Active cortical dendrites modulate perception. Science *354*, 1587–1590.

Taube, J.S. (2007). The head direction signal: origins and sensory-motor integration. Annu. Rev. Neurosci. *30*, 181–207.

Taube, J.S., Muller, R.U., and Ranck, J.B., Jr. (1990). Head-direction cells recorded from the postsubiculum in freely moving rats. I. Description and quantitative analysis. J. Neurosci. *10*, 420–435.

Voigts, J., Siegle, J.H., Pritchett, D.L., and Moore, C.I. (2013). The flexDrive: an ultra-light implant for optical control and highly parallel chronic recording of neuronal ensembles in freely moving mice. Front. Syst. Neurosci. *7*, 8.

Williams, S.R., and Fletcher, L.N. (2019). A dendritic substrate for the cholinergic control of neocortical output neurons. Neuron *101*, 486–499.e4.

Xu, N.L., Harnett, M.T., Williams, S.R., Huber, D., O'Connor, D.H., Svoboda, K., and Magee, J.C. (2012). Nonlinear dendritic integration of sensory and motor input during an active sensing task. Nature *492*, 247–251.

Xu, Y., Zou, P., and Cohen, A.E. (2017). Voltage imaging with genetically encoded indicators. Curr. Opin. Chem. Biol. *39*, 1–10.

Yang, X., Zhou, T., Zwang, T.J., Hong, G., Zhao, Y., Viveros, R.D., Fu, T.-M., Gao, T., and Lieber, C.M. (2019). Bioinspired neuron-like electronics. Nat. Mater. *18*, 510–517.

Yilmaz, M., and Meister, M. (2013). Rapid innate defensive responses of mice to looming visual stimuli. Curr. Biol. *23*, 2011–2015.

Yoon, K., Lewallen, S., Kinkhabwala, A.A., Tank, D.W., and Fiete, I.R. (2016). Grid cell responses in 1D environments assessed as slices through a 2D lattice. Neuron *89*, 1086–1099.

Zhang, Z., Russell, L.E., Packer, A.M., Gauld, O.M., and Häusser, M. (2018). Closed-loop all-optical interrogation of neural circuits in vivo. Nat. Methods *15*, 1037–1040.

Zhou, M., Liang, F., Xiong, X.R., Li, L., Li, H., Xiao, Z., Tao, H.W., and Zhang, L.I. (2014). Scaling down of balanced excitation and inhibition by active behavioral states in auditory cortex. Nat. Neurosci. *17*, 841–850.

Zong, W., Wu, R., Li, M., Hu, Y., Li, Y., Li, J., Rong, H., Wu, H., Xu, Y., Lu, Y., et al. (2017). Fast high-resolution miniature two-photon microscopy for brain imaging in freely behaving mice. Nat. Methods *14*, 713–719.

STAR★METHODS

KEY RESOURCES TABLE

REAGENT or RESOURCE	SOURCE	IDENTIFIER
Bacterial and Virus Strains		
AAV2/1-hSyn-GCaMP6f	Chen et al., 2013b, https://www.addgene.org/100837/	100837-AAV1
Experimental Models: Organisms/Strains		
Mice: C57BL/6	https://www.jax.org/strain/000664	000664
Software and Algorithms		
Image de-rotation algorithm	This paper	https://github.com/jvoigts/rotating-2p-image-correction
Non-rigid motion correction method	Pnevmatikakis and Giovannucci 2017	https://github.com/flatironinstitute/NoRMCorre
Open ephys data acquisition software	https://Open-ephys.org	https://github.com/open-ephys/plugin-GUI
Simpleclust spike sorting software	https://Open-ephys.org	https://github.com/open-ephys/simpleclust
MATLAB	Mathworks	https://www.mathworks.com/products/matlab.html
Other		
Rotating head-fixation system	This paper	
Tetrode drive implants	Voigts et al., 2013	https://github.com/open-ephys/shuttle-drive
LED driver	Newman et al., 2015	https://github.com/jonnew/cyclops

LEAD CONTACT AND MATERIALS AVAILABILITY

Further information and requests for resources and reagents should be directed to and will be fulfilled by the Lead Contact, Mark T. Harnett (harnett@mit.edu). This study did not generate new unique reagents.

EXPERIMENTAL MODEL AND SUBJECT DETAILS

Mice (C57BL/6) were aged 8-15 weeks at the time of surgery. Animals were individually housed and maintained on a 12-h cycle. Animals of either sex were used. All experiments were conducted in accordance with the National Institutes of Health guidelines and with the approval of the Committee on Animal Care at the Massachusetts Institute of Technology (MIT).

METHOD DETAILS

Mechanical system

Headpost clamp: We used an adapted standard headpost and clamp (Andermann et al., 2013; Goldey et al., 2014). The headpost clamp is engineered so it can be tightened or released with a single thumbscrew allowing easy insertion or removal of mice with one hand. Strain gage frame: An aluminum frame connects the headpost clamp to an array of 2 strain gages (Phidgets Inc. load cells, See Figures 1 and S1B–S1D) that are set up as an opposing pair to not register any forces other than torque around the rotation axis. The torque is measured via a battery powered instrumentation amplifier and transmitted via a wireless link (SparkFun RFM69) to the main micro-controller (PRJC Teensy 3.6). Rotating frame: The strain gages are held in a rotating frame that is made from milled aluminum on a flat waterjet cut base plate (1/4'' aluminum). This rotating frame also holds all rotating amplifiers, control electronics, wireless link, and a battery system. A 5V rechargeable lithium ion external cell phone battery with ~5000mAh is used to power the microcontroller and amplifiers. The frame also includes a bearing carrier surface for a thin profile bearing (Kaydon K13008XNOK), and a sprocket ring for the drive belt. Air maze system: The maze that the animals walk on needs to be translationally friction free and have low inertia (Kislin et al., 2014; Nashaat et al., 2016), but cannot be allowed to rotate. The air maze itself is a circular, or otherwise shaped arena of ~25 cm diameter, which floats on an air cushion providing animals with the ability to walk without experiencing resistance. The air maze floor is made from carbon fiber sheet. Crucially, the air maze needs to be restricted from spinning on its own, so that all torques exerted by the animals are transferred to the headpost and can be compensated there. For this purpose, the arena has a protruding constraint pin that fits through a corresponding guide (precisely, a pair of guides, see Figure S1E) on the constraint system shuttle, acting as a linear bearing: the guide pin can slide in and out of this bearing, allowing the arena to move in the x direction (Figure S1F). In order to allow y-direction motion, the system measures the torque or angle with which the guide pin enters the bearing, and actively keeps the angle between the constraint shuttle and the guide pin at 90 degrees. The shuttle therefore constantly follows the arena in

the y direction if the arena translated, but rotational torque does not move the shuttle and is absorbed by the rigid constraint system. Because the air maze does not rotate, electricity and signal wires can easily be routed through the guide pin, or by slack lightweight wires or tubes, needing no commutation. The motion of the arena is tracked with an IR LED driven by an adjustable current source (Newman et al., 2015) that is attached to the arena and is tracked with a pixy camera (Nashaat et al., 2017). The air maze floats on an air cushion provided by a large air table made from two 30 × 30'' sheets of clear acrylic, the top of which has a pattern of small holes drilled. The space between the acrylic sheets is pressurized with air. A series of threaded rods tie the two sheets together to ensure that the distance between the acrylic plates stays constant. Bridge frame and motor: The static bridge frame holds a bearing carrier surface for the main bearing, the base plate that forms the non-moving 'ceiling' that is seen by the animals, and can be covered with a mirrored surface or fitted with screens for display of a VR environment. The bridge frame also carries the drive motor and motor control electronics. The whole bridge frame is hinged along the short side opposite to the motor, allowing it to can be tilted upward, facilitating insertion and removal of animals. The main microcontroller receives torque data from the rotating frame system at ~500 Hz and computes the required motor torque. The rotating frame is driven via a Gates GT2 belt from a brushless motor (Teknic Clearpath) mounted on one side of the bridge frame. The motor is controlled by a separate microcontroller via a simple PWM torque command. The microcontroller also reads the position of the motor encoder in order to track the heading of the mouse. The controller then sends this heading to the host PC via a stream of serial data.

Force feedback control system

The feedback system (Figures 1B and S1D) is implemented on a PRJC Teensy 3.6 micro-controller (32 bit 180 MHz ARM Cortex-M4 processor, floating point unit). The control loop time is determined by the speed at which torque data is transmitted from the headstage controller and runs at around 1.5-1.8kHz. The system aims to keep the torque at the headpost as close to zero as possible. The principal control scheme is a proportional feedback with a gain of around 2000, so a static torque of 1 mNm would cause the motor to exert around 2 Nm of torque to the headpost frame in the same direction. In broad terms, a light touch on one side of the headpost mount results in a torque amplification that is hard to resist when holding the headpost frame with the other hand. This amplified torque has the effect of reducing the apparent weight of the headpost frame, so it can be effortlessly rotated by a mouse. Due to the imperfections of the mechanical system, a few additional control elements work in concert with this proportional feedback gain: the zero-point of the strain gages is calibrated for each session, and thermal drift of the strain gages is continuously zeroed out by a slowly changing separate calibration offset (max. of 5% of the strain gage dynamic range every minute). The gain decreases with the frequency of the signal, rolling off at around 20Hz to avoid positive feedback from mechanical vibrations of the bridge frame. The overall system gain is slowly ramped on at the beginning of a session, and safety interlocks stop the system when the instantaneous torque, or absolute angular motion within a 100ms window reaches thresholds that exceed normal mouse motion. These values were set empirically so that they are slightly above values achieved by mice when navigating. Finally, the friction in the bearing system increases when the bearing is static, which means that the gain can be slightly higher when the bearing is at rest. This is implemented with an additional gain factor of 1.2 that linearly drops to 0 at a speed of ~3RPM.

Surgery

Mice (C57BL/6) were aged 8-15 weeks at the time of surgery. Animals were individually housed and maintained on a 12-h cycle. All experiments were conducted in accordance with the National Institutes of Health guidelines and with the approval of the Committee on Animal Care at the Massachusetts Institute of Technology (MIT). All surgeries were performed under aseptic conditions under stereotaxic guidance. Mice were anesthetized with isofluorane (2% induction, 0.75%–1.25% maintenance in 1 l/min oxygen) and secured in a stereotaxic apparatus. A heating pad was used to maintain body temperature, additional heating was provided until fully recovered. The scalp was shaved, wiped with hair-removal cream and cleaned with iodine solution and alcohol. After intraperitoneal (IP) injection of dexamethasone (4 mg/kg), Carprofen (5mg/kg), subcutaneous injection of slow-release Buprenorphine (0.5 mg/kg), and local application of Lidocaine, the skull was exposed. The skull was cleaned with ethanol, and a base of adhesive cement (C&B Metabond) was applied.

Chronic headpost and imaging window implants were performed over central midline cortex. A 3 mm craniotomy was drilled, 4 to 6 injections of ~50nl each of AAV2/1-hSyn-GCaMP6f (~10^12 viral molecules per ml) (Chen et al., 2013b), were made bilaterally, around 0.3-0.6mm from the midline at depths of ~500 μm, and a cranial window (Andermann et al., 2011; Goldey et al., 2014) 'plug' was made by stacking two 3 mm coverslips (Deckgläser, #0 thickness (~0.1 mm); Warner; CS-3R) under a 5mm coverslip (Warner; CS-5R), using optical adhesive (Norland Optical #71). The plug was inserted into the craniotomy and the edges of the larger glass were sealed with Vetbond (3M) and cemented in place. The dura was left intact. Mice were given 2 weeks to recover and for virus expression before the start of recordings.

Chronic drive implants (Figure 2A) were performed identically to the window implants, but instead of a 3mm craniotomy for a glass window, a 2mm craniotomy was drilled ~2mm lateral and ~0.5mm anterior of the transverse sinus. A durotomy was performed, and tetrode drives (Voigts et al., 2013) were implanted and fixed with dental cement.

Chronic Electrophysiology

To verify head-direction encoding, we used conventional tetrode array recordings (Voigts et al., 2013), targeting postsubiculum, where cells encode combined spatial and head-direction direction (Taube et al., 1990). After implant surgery, Individual tetrodes

were lowered over the course of multiple days until head-direction cells in postsubiculum could be identified by their tuning profiles (Peyrache et al., 2015; Taube et al., 1990). Data were acquired with an Open Ephys system (Siegle et al., 2017) at 30kHz, and spikes were sorted manually from 300-6000Hz band pass filtered voltage traces. We first let mice explore a circular arena (25cm diameter) with visual cues glued to the walls for ~15 min while recording spike trains and measuring the mouse's position with a camera. The mouse's head direction was tracked from the video data. The same mouse was then transferred to the rotating head-fixed system, and a second recording session was carried out. Spike sorting was carried out after concatenating the two sessions, and all sorted cells were maintained across the sessions. We included cells with a modulation depth by heading of at least 20%, defined as $100*((rate_{max}-rate_{min})/rate_{max})$ in the analysis.

2-Photon imaging

All imaging data were acquired at a frame rate of 9-11Hz using a 2-photon microscope with a combined resonant scanner/galvo system (Neurolabware, Los Angeles, CA). Imaging was performed with an excitation wavelength of 980nm, coupled to a 4x passive pulse splitter to reduce photobleaching (Ji et al., 2008). Two imaging planes (~20-60μm depth for apical dendrite segments and ~350-500μm for soma and trunk dendrites) were scanned alternatively via an electrically tunable lens (ETL, Optotune EL-10-30) that was positioned just before the resonant/galvo scanner. The ETL was driven with a custom waveform that drove fast plane transitions but avoided oscillations and included a slower component to eliminate any slower settling after the transitions, which would otherwise result in image plane tilt. The rotation of the animal was read out from the drive motor's encoder at a frequency of 500Hz, which provides enough time-resolution to determine the rotation for each individual scan line of the image series, and was saved with the imaging data.

Prior to each imaging session, the axial position of the microscope relative to the rotation axis of the headpost was calibrated by mounting a calibration target in the headpost holder to stand in for the mouse. The headpost was then rotated slowly via the motor, and the 2-photon miscroscope was centered over the axis of rotation by visual inspection of the rotating target. By imaging the target at high magnification, the axis could easily be aligned to within ~2 micron. The same target was used to ensure that the imaging Z-plane was stable to within ~2 micron throughout the full range of rotation.

De-rotation

The imaging data recorded while the animal rotates is rotated relative to the scan system of the microscope, and therefore distorted. The distortion results from the fact that the image acquisition is not instantaneous, so that the top line of a frame will be acquired at a different time, and possibly at a different angle of rotation, from the bottom line etc. (Figure 1C). In mild cases this results in an apparent curving of the image, theoretically it can lead to parts of the field of view getting imaged twice per frame. We have developed a computational method for correcting these distortions. The method functions by computing the exact rotation of each scan line by interpolating the motor position, computing the 'forward' model of the distortion by generating a map of the x and y displacements per pixel by recapitulating the scan using the known scan pattern and the measured animal rotation for each image line. The resulting displaced x/y positions of each original x/y pixel are then used to reverse the deformation (Figures 1C and 1D). After this correction step, images are processed with a standard motion correction pipeline (Pachitariu et al., 2017; Pnevmatikakis and Giovannucci, 2017; Pnevmatikakis et al., 2016). After motion correction, ROIs of individual cells and dendrite segments are identified manually using custom software and $\Delta F/F_0$ traces are computed. After derotation, the systematic phase offset was removed by applying a linear phase shift in the spectral domain and then transforming the signal back to the time domain.

Correction of uneven illumination

If the illumination of the FOV is not completely even, due to small deviations of the laser alignment from the objective or rotation axes or from non-uniform back-aperture illumination of the objective, rotation of the animal will bring imaged structures in and out of areas of higher or lower brightness. In our data, this effect accounted for only ~10%–20% of ROI brightness for ROIs near the center of the field of view, approximately the center 50% of max FOV. To resolve this artifact we adapted the method typically used for correction of baseline fluorescence (Chen et al., 2013b): Typically, for each ROI, a baseline fluorescence F_0 is computed as a low (usually 5-40th) percentile of either all fluorescence data for a session, a pre-stimulus period, or in a moving window of a minute or more. This F_0 is then used as a baseline and the time series $\Delta F/F_0$ is used for subsequent analyses. Here, we used a similar method, but F_0 is computed not over time, but across angles (Figure S5) by computing a quantile for each angle first. On our experiments, this simple approach sufficiently corrected the angle dependent brightness changes (Figures S5C and S5D). We then applied neuropil correction by estimating the mixing of a background ROI devoid of any Ca^{2+} transients on each ROI with a linear fit to the lowest 10th percentile, and subtracting the neuropil data with this coefficient. As an additional control, we removed ROIs where no Ca^{2+} transients were evident over large > 60degree ranges of rotation for entire imaging sessions, as those ROIs could possibly have originated from cell bodies whose visibility might have been occluded in an angle-dependent manner by superficial blood vessels (Figures S3E and S3F).

Identification and classification of Ca^{2+} transients

Pairs of soma and dendrite ROIs were manually associated by using sparse activity in series of fast z stacks (Figure S4). The resulting associated dendritic and somatic Ca^{2+} traces are referred to as 'pairs'. The dendritic and somatic traces are amplitude matched by

their peak amplitudes, and the traces were then smoothed (σ = 3 frames, ~0.5 s). Ca^{2+} events were detected by first estimating the local noise distribution and then detecting deviations that exceed this distribution. In order to avoid biases due to the sparse but large Ca^{2+} transients, we used quantiles rather than averages to estimate the noise floor: For each sample of both the top and the bottom trace, a separate probability of that sample being noise is computed by fitting a Gaussian distribution to the noise by quantiles (mean = 40^{th} percentile, std = range of 10^{th} to 90^{th} percentiles). This fitting procedure captures the statistics of the background noise in the GCaMP traces but is unaffected by transients or firing rate differences. The overall noise probability is then defined as the product of the dendritic and somatic noise probabilities (close to 1 for noise, close to 0 for signals exceeding the noise floor, See Figure S4D). This product implements an 'or' function, where events originating from either the soma or dendrite are detected in an unbiased manner. Event onsets are defined as P(noise) values under 0.2 and offsets as increases over 0.7. Events are then classified as local dendritic or local somatic if they are significantly driven by only one of the signals, and joint otherwise. To perform this classification, the somatic versus dendritic signals (in the normalized data) are compared per event. For each event, the 25^{th} percentile of the difference between the normalized dendritic and somatic $\Delta F/F_0$ signals throughout the event is computed. If this difference exceeds > 0.01, and if the somatic signal quantile stays below 0.05, the transient is labeled as local dendritic. The reverse criterion is applied to identify local somatic events: if the somatic signal is bigger (difference < −0.02), and the quantile of the dendritic signal is below 0.02, it is labeled as somatic. All remaining events, with contributions from both the soma and dendrite, are labeled as 'joint'.

QUANTIFICATION AND STATISTICAL ANALYSIS

Unless otherwise noted, all statistical tests are computed two-sided as Wilcoxon rank sum tests when samples are independent or as signed rank tests when the samples are paired. No statistical methods were used to predetermine sample size. The investigators were not blinded to allocation during experiments and analysis. Distributions of measurements are plotted as histograms, normalized via the sum, so that the sum of the entire plotted histogram is 1. The x/y position of the mouse was computed from the raw tracking data by an affine transform to remove the camera distortion and occasional obvious tracking errors were removed by interpolating over individual frames with a position jump of > 5cm. The x/y data were then median filtered with a 3-bin window to reduce jitter, and down-sampled and aligned to the Ca^{2+} data. Head direction (HD) data were available at 500Hz with virtually no noise directly from the motor controller and were simply down-sampled. In some cases, only a subset of soma-dendrite pairs where a certain threshold of Ca^{2+} events was observed was analyzed, such as for the analysis of tuning differences, and the selection criteria are stated in the figure. The Ca^{2+} timescales were measured by fitting an exponential decay function to the time segment between the peak of each transient (defined on a smoothed copy of the trace to increase robustness, σ = 2 frames), and the end of the transient, defined as return to 0, and the decay time constant τ is reported as positive numbers. For comparisons of local versus joint event amplitudes, the mean amplitudes of local and joint events were compared per pair. The same result can be seen if the mean joint event amplitude was computed for each pair, and the difference of individual local events versus that mean amplitude are reported (N = 985, $p < 0.001$). To compute the spatial and head-direction (HD) tuning, event rates were computed by dividing event count by occupancy in an 8x8 grid for the position, and 40 bins, circularly smoothed with σ = 0.075 radians for HD, excluding times when the mouse was stationary. To compute the information content of the tuning, the entropy of the distributions was computed as the Kullback–Leibler (KL) divergence between the distribution of rates and the distribution of occupancy, giving a measure of whether and how much additional information is contained in the firing rate pattern. Zero and negative values indicate cells that do not contain rate information in that dimension. To compute an unbiased comparison between the tuning of dendrite segments and their soma, the joint and local dendritic events were converted to rate-matched point processes, by sampling events from the (more numerous) joint events to match the number of local events. Now the tuning of local events was first compared to itself by splitting the data in half. This comparison gives a baseline difference that captures the variance /reliability of the encoding by the dendritic signal, against which another signal can be compared. The dendritic coding is compared to that of the (rate matched) parent soma, across the same split (Figure 5E), so that both comparisons are done from one dendritic signal to dendritic and somatic signals captured simultaneously, resulting in an unbiased comparison of the dendritic to somatic tuning, taking the tuning reliability into account. The comparison was carried out by computing the tuning as described before, and calculating the difference as the 2-norm, $|tuning_1 - tuning_2|$.

DATA AND CODE AVAILABILITY

Code generated during this study is available at https://github.com/jvoigts/rotating-2p-image-correction. Datasets generated in the current study are available from the corresponding author on request.